Accepted Manuscript

Material distribution and sizing optimization of functionally graded plate-shell structures

José S. Moita, Aurélio L. Araújo, Victor Franco Correia, Cristóvão M. Mota Soares, José Herskovits

PII: S1359-8368(17)33934-3

DOI: 10.1016/j.compositesb.2018.01.023

Reference: JCOMB 5514

To appear in: *Composites Part B*

Received Date: 13 November 2017

Revised Date: 2 January 2018

Accepted Date: 22 January 2018

Please cite this article as: Moita JoséS, Araújo AuréL, Correia VF, Mota Soares CristóãM, Herskovits José, Material distribution and sizing optimization of functionally graded plate-shell structures, *Composites Part B* (2018), doi: 10.1016/j.compositesb.2018.01.023.

Material Distribution and Sizing Optimization of Functionally Graded Plate-Shell Structures

José S. Moita [a], Aurélio L. Araújo [a], Victor Franco Correia [b, 1], Cristóvão M. Mota Soares [a], José Herskovits [c,d]

[a] IDMEC, Instituto Superior Técnico, Universidade de Lisboa
Av. Rovisco Pais, 1049-001 Lisboa, Portugal

[b] Escola Superior Náutica Infante D. Henrique,
Av. Eng. Bonneville Franco, 2770-058, Paço de Arcos, Portugal

[c] COPPE-UFRJ, Universidade Federal do Rio de Janeiro, Brazil
[d] Department of Mechanical and Materials Engineering
Military Institute of Engineering, Rio de Janeiro, Brazil

Keywords: Functionally Graded Materials, FGM Plates, FGM Shells, Optimization.

Abstract

A high order shear deformation theory is used to develop a discrete model for the structural and sensitivity analyses allowing for the material distribution and sizing optimization of functionally graded material (FGM) structures. The finite element formulation for general FGM plate-shell type structures is presented, and a non-conforming triangular flat plate/shell element with 24 degrees of freedom for the generalized displacements is used. The formulation accounts for geometric and material nonlinear behaviour, free vibrations and linear buckling analyses, and their analytical gradient based sensitivities. The p-index of the power–law material distribution and the thickness are the design variables. Mass, displacement, fundamental frequency and critical load are the objective functions or constraints. The optimization solutions, obtained by a Feasible Arc Interior Point gradient-based algorithm, for some plate-shell examples are presented for benchmarking purposes.

1. Introduction

In an effort to develop the super heat resistant materials, Koizumi [1] first proposed the concept of Functionally Graded Material (FGM). Typical FGM plate-shell type structures are made of materials characterized by a continuous variation of the material properties over the thickness direction by mixing two different materials, metal and ceramic. The metal–ceramic FGM plates and shells are widely used in aircraft, space vehicles, reactor vessels, and other engineering applications.

Structures made of composite materials have been widely used to satisfy high performance demands. In such structures, stress singularities may occur at the interface between two different materials. In contrast, in FGM plate-shell structures the smooth and continuous variation of the properties from one surface to the other eliminates abrupt changes in the stress and displacement distributions.

[1] Corresponding author: victorfranco@enautica.pt

In certain applications, structures can experience large elastic deformations and finite rotations. Geometric nonlinearity plays a significant role in the behaviour of a plate or shell structures, especially when it undergoes large deformations. In addition, material nonlinearity has a significant role in the behaviour of these structures.

Significant research in FGM structures has been done in the recent years, but only a few works could be found involving the optimization of these type of structures and much less involving the optimization of these structures considering nonlinear behaviour. The authors, Moita et al. [2] have published recently a paper where static nonlinear analysis was investigated and in another work, Moita et al. [3], have addressed the linear buckling of these structures. In both these works, the authors have mentioned a significant number of references which have been considered in the formulation and for comparison of results. In the present paper, only a few of those works will be mentioned as follows. Reddy and Arciniega [4] presented free vibration analysis of FGM plates. The same authors [5] carried out the large deformation analysis of FGM shells. Kim et al. [6] presented the geometric nonlinear analysis of functionally graded material plates and shells using a four-node quasi-conforming shell element. Zhao and Liew [7] analyzed the nonlinear response of functionally graded ceramic–metal shell panels under mechanical and thermal loading, using a displacement field expressed in terms of a set of mesh-free kernel particle functions. Ramu and Mohanty [8] applied the finite element method, using the classical plate theory, for the modelling and buckling analysis of FGM rectangular plates, under uniaxial and biaxial compression loads along with simply supported boundary conditions.

Recently, some new models were developed [9,10,11,12] dealing with nano and FGM structures. These models could be extend to contemplate structural optimization.

Regarding the structural optimization involving FGM plates and shells there is a lack of publications specifically devoted to this subject. The following recent works can be mentioned, among others:

Cho et al [13] have applied artificial neural network (ANN) to the material composition optimization of heat-resisting functionally graded materials (FGMs).

Chen et al [14] have presented a numerical technique for performing sensitivity analysis of coupled thermomechanical problems involving FGMs, where the design variables were the volume fractions of the constituents and structural shape parameters and the design optimization problem solved by the sequential linear programming.

Goupee et al [15] have proposed a methodology for the multi-objective optimization of material distribution in FGMs, with temperature-dependent material properties for steady thermomechanical processes for metal/ceramic and metal/metal, based in a Genetic Algorithm.

Goupee at al [16] have combined an optimization scheme where in a first problem, the peak residual stress is minimized when the functionally graded component is cooled from a high fabrication temperature and in a second problem the mass of a graded component is minimized with constraints on the peak effective stress and maximum temperature experienced by the metal.

Vel et al [17] have proposed a methodology for the multi-objective optimization of material distribution of FGM cylindrical shells for steady thermomechanical processes where the volume fractions at the control points were chosen as the design variables and were optimized using an elitist, non-dominated sorting multi-objective Genetic algorithm.

Xia et al [18] proposed for the simultaneous optimization of the material properties and the topology of FGM structures, determining the optimal volume fractions of the materials and the structural topology to maximize the performance of the structure, by using sensitivity analysis to obtain the descent directions.

Na et al [19] have performed the volume fraction optimization of FGM composite panels by considering stress reduction and thermo-mechanical buckling behaviour improvement.

Mozafari et al [20] have presented an Imperialist Competitive Algorithm, an universal search strategy that was inspired by the concept of socio-political competition among empires, for optimizing the critical buckling load on plates made of FGM plates with variable thickness.

Kou et al [21] proposed a particle swarm optimization method to optimize FGM structures and compared with classical mathematical programming based optimizers.

Noh et al [22] have noted that nowadays the capacity of the manufacturing techniques of FGM may not yield the target volume fraction and to deal with that uncertainty in the manufacturing process a so-called reliability-based design optimization for FGM was presented involving design of experiments and considering the volume fractions of homogenized FGM layers and material properties as design variables.

Vatanabe et al. [23] have proposed a methodology, based on topology optimization and homogenization, to the optimal design of FGM piezocomposites for energy harvesting applications considering the influence of piezoelectric polarization directions and the influence of material gradation.

Ashjari et al [24] performed the optimization of material distribution in FGM plates where the volume fractions at control points were selected as design variables, using two evolutionary algorithms: Real-coded genetic algorithm; and particle swarm optimization algorithm.

Loja [25] has studied the use of particle swarm optimization technique for the maximization of the bending stiffness of a FGM sandwich beam, using symbolic computation.

Taheri et al [26] presented the eigenfrequency optimization of FGM structures within the framework of isogeometric analysis (IGA) combining the shape and material composition optimization.

Taheri et al [27] presented an isogeometrical procedure for optimization of material composition of FGM plates allowing for the gradation of material properties through patches, considering the volume fractions of the constituents as the design variables and solving the optimization problem using mathematical programming.

Wang et al [28] have studied the FGM design optimization of pressure vessels subjected to thermo-mechanical loading by using the ANSYS parametric design language.

Shi et al [29] have presented a shape optimization method for designing functionally graded (FG) sandwich structures with two different materials to minimize the compliance of these structures under a volume constraint, using the material derivative and adjoint methods. FG sandwich structures with two sets of metal–ceramic materials, aluminium–alumina and aluminium–zirconia, were given as examples to verify the validity of the method.

Roque et al. [30] have used a differential evolution optimization technique to find the volume fraction that maximizes the first natural frequency of FGM beams.

Very recently, Tsiatas et al [31] have employed a Differential Evolution technique for optimizing the natural frequencies of axially FG beams and arches. The evaluation of the objective function required the solution of a free vibration problem of an arch with variable mass and stiffness properties, where the arches were modelled using a generic curved beam model that includes both axial and transverse deformation and the problem was solved using the analogue equation method (AEM) for hyperbolic differential equations with variable coefficients.

Shabana et al [32] have used particle swarm optimization technique to minimize the induced stresses in FGM cylinders subjected to pressure loading, where the design variables were volume fractions of the constituent materials.

Andrianov et al [33] have performed a strain analysis and optimal design of FGM rods and beams with small inclusions using a homogenization procedure.

Lieu et al [34] have presented a numerical approach for modeling and optimizing the ceramic volume fraction distribution of FGM plates subject to thermo-mechanical loadings employing an adaptive hybrid evolutionary firefly algorithm to solve compliance minimization problems with volume constraints.
Hao Li et al [35] have developed a topology optimization method for the computational design of functionally graded cellular composites hosting auxetic metamaterials.
Franco et al [36] developed a multiobjective design optimization scheme for ceramic–metal FGM plates with properties varying through the thickness direction, where constrained optimization is conducted for different behaviour objectives like the maximization of buckling load or fundamental natural frequency, mass minimization and material cost minimization. The constraints were stress based failure criteria and other structural response constraints or manufacturing limitations and the design variables were the index of the power-law distribution in the metal-ceramic graded material and the thicknesses of the graded material and/or the metal and ceramic faces and the optimization problems were solved with two direct search derivative-free algorithms.

The mechanical properties of FGMs are dependent of the p-index of the power-law that defines the volume fraction of the ceramic phase. Thus, the FGM structures could be designed to meet the specific requirements of each particular application. Accurate and efficient structural analysis, design sensitivity analysis and optimization procedures are of fundamental importance to accomplish this task. The objective of this work is to present the development of analytical sensitivities for FGM structures, following the work of Moita et al. [37], and previous works, [2] and [3], and to present some benchmarking optimization applications of plate-shell structures by using the Feasible Arc Interior Point gradient-based algorithm.

2. Formulation of FGM Model

A FGM can be made by mixing two distinct isotropic material phases, for example a ceramic and a metal. The material properties of an FGM plate/shell structures are assumed to change continuously throughout the thickness, according to the volume fraction of the constituent materials. Power-law function [38] and exponential function [39] are commonly used to describe the variations of material properties of FGM. However, in both power-law and exponential functions, the stress concentrations appear in one of the interfaces in which the material is continuously but rapidly changing. Therefore, Chung and Chi [40] proposed a sigmoid FGM, which was composed of two power-law functions to define a new volume fraction. Chi and Chung [41] indicated that the use of a sigmoid FGM could significantly reduce the stress intensity factors of a cracked body. To describe the volume fractions, the power-law function is used here.

2.1 Power-law function

The volume fraction of the ceramic phase is defined according to the power-law [40]:

$$V_c(z) = \left(0.5 + \frac{z}{h}\right)^p \tag{1}$$

$$V_m(z) = 1.0 - V_c(z) \tag{1a}$$

being $z \in (-h/2; h/2)$, h the thickness of structure, and the exponent p a parameter that defines the gradation of material properties across the thickness direction.

In the present work, the continuous variation of the materials mixture is approximated by the using a certain number of virtual layers throughout the thickness direction - layer approach. In this sense, the previous equations can be written for each virtual layer as follows:

$$V_c^k = \left(0.5 + \frac{\bar{z}_k}{h}\right)^p \quad ; \quad V_m^k = 1.0 - V_c^k \tag{2}$$

where $\bar{z}_k$ is the thickness coordinate of mid-surface of each layer.

Once the volume fraction V_c^k and V_m^k have been defined, the material properties (H) of each virtual layer of an FGM can be determined by the rule of mixtures

$$H^k = V_c^k H_c + V_m^k H_m \tag{3}$$

where H denotes the Young's modulus E, the Poisson's ratio υ, the mass density ρ, or any other mechanical property.

Figure 1 shows the variation of Young's modulus E through the thickness, obtained using the power-law function and a 20 layer approach for the approximation through the thickness.

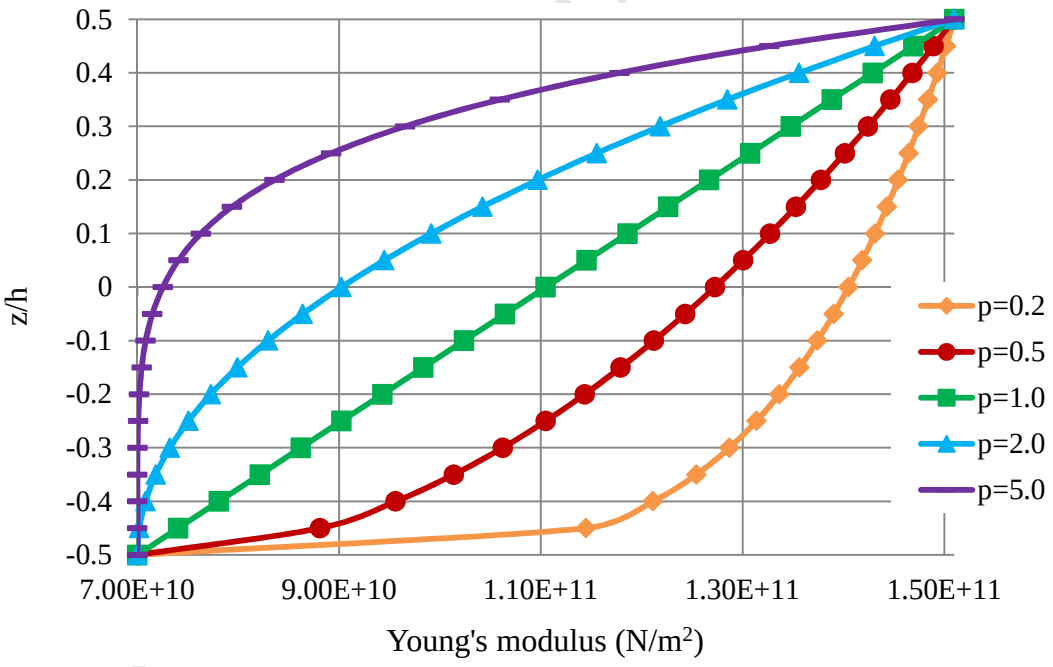

Figure 1. Variation of Young's modulus (N/m^2) through the thickness, obtained using the power-law function and a 20 layer approach

3. Displacement Field, Strains and Constitutive Relations

The present theory considers large displacements with small strains. The displacement field is based on the Reddy's third-order shear deformation theory [42]:

$$u(x,y,z) = u_0(x,y) - z\,\theta_y(x,y) + z^3\,c_1\left[\theta_y(x,y) - \frac{\partial w_0}{\partial x}\right]$$
$$v(x,y,z) = v_0(x,y) + z\,\theta_x(x,y) + z^3\,c_1\left[-\theta_x(x,y) - \frac{\partial w_0}{\partial y}\right]$$
$$w(x,y,z) = w(x,y) \qquad (4)$$

where u_0, v_0, w_0 are displacements of a generic point in the middle plane of the core layer referred to the local axes in the *x,y,z* directions respectively, θ_x, θ_y are the rotations of the normal to the middle plane, about the *x* axis (clockwise) and *y* axis (anticlockwise), $\partial w_0/\partial x, \partial w_0/\partial y$ are the slopes of the tangents of the deformed mid-surface in *x,y* directions, and $c_1 = 4/3\,h^2$, with h denoting the total thickness of the structure.

The stress-strain relations for each layer k, can be written as follows

$$\boldsymbol{\sigma}_k = \mathbf{Q_k}\ \boldsymbol{\varepsilon}_k \qquad (5)$$

where $\boldsymbol{\sigma}_k = \{\sigma_x\ \sigma_y\ \sigma_{xy}\ \tau_{xz}\ \tau_{yz}\}^T$ is the stress vector and $\boldsymbol{\varepsilon}_k = \{\varepsilon_x\ \varepsilon_y\ \gamma_{xy}\ \gamma_{xz}\ \gamma_{yz}\}^T$ is the strain vector, $\mathbf{Q}_k$ is the elasticity matrix, given by:

$$\mathbf{Q}_k = E_k \begin{bmatrix} \frac{1}{1-\nu^2} & \frac{\nu}{1-\nu^2} & 0 & 0 & 0 \\ \frac{\nu}{1-\nu^2} & \frac{1}{1-\nu^2} & 0 & 0 & 0 \\ 0 & 0 & \frac{1}{2(1+\nu_k)} & 0 & 0 \\ 0 & 0 & 0 & \frac{1}{2(1+\nu_k)} & 0 \\ 0 & 0 & 0 & 0 & \frac{1}{2(1+\nu_k)} \end{bmatrix} = E_k\ \mathbf{c} \qquad (6)$$

For each layer, the linear elastic constitutive equation is given by [43]:

$$\hat{\boldsymbol{\sigma}}_k = \hat{\mathbf{D}}_k\ \boldsymbol{\varepsilon}^0_\kappa \qquad (7)$$

where $\hat{\boldsymbol{\sigma}}_k$ are the resultant forces and moments, and $\hat{\mathbf{D}}_k$ the constitutive matrix. The previous equation can be written as

$$\hat{\boldsymbol{\sigma}} = \sum_{k=1}^{N} \mathbf{Q}_k\ \frac{z^n_{k+1} - z^n_k}{n}\ \boldsymbol{\varepsilon}^0_\kappa \quad . \qquad (8)$$

In this work, geometrically non-linear behaviour of FGM plate/shell type structures under mechanical loading is also considered. To the geometrically nonlinear behaviour, the Green's strain tensor is here considered. Its components are conveniently represented in terms of the linear and nonlinear parts of the strain tensor as

$$\boldsymbol{\varepsilon}_k = \left\{ \boldsymbol{\varepsilon}_k^{L} + \boldsymbol{\varepsilon}_k^{NL} \right\} \tag{9}$$

The linear strain components associated with the displacement field given above, can be represented in a synthetic form:

$$\boldsymbol{\varepsilon}_k^{L} = \begin{Bmatrix} \boldsymbol{\varepsilon}_{m_K}^0 + \overline{z}_k \, \boldsymbol{\varepsilon}_{bK}^0 + \overline{z}_k^3 \, \boldsymbol{\varepsilon}_{*b_K}^0 \\ \boldsymbol{\varepsilon}_{sk}^0 + \overline{z}_k^2 \, \boldsymbol{\varepsilon}_{*sK}^0 \end{Bmatrix} \tag{10}$$

where $\boldsymbol{\varepsilon}_{mk}^0, \boldsymbol{\varepsilon}_{b_k}^0, \boldsymbol{\varepsilon}_{*b_k}^0, \boldsymbol{\varepsilon}_{s_k}^0, \boldsymbol{\varepsilon}_{*s_k}^0$ are, respectively, the vectors of membrane strain, bending strain, shear strain and also the vectors of bending strain and shear strain associated with third-order terms. For example, in direction x they are explicitly given by:

$$\varepsilon_m^0 = \frac{\partial u_0}{\partial x}; \; \varepsilon_b^0 = \frac{\partial \theta_y}{\partial x}; \; \varepsilon_{*b}^0 = c_1 \left(\frac{\partial \theta_y}{\partial x} - \frac{\partial^2 w_0}{\partial x^2} \right); \; \varepsilon_s^0 = -\theta_y + \frac{\partial w_0}{\partial x}; \; \varepsilon_{*s}^0 = c_2 \left(-\theta_x - \frac{\partial w_0}{\partial y} \right) \tag{11}$$

where $c_2 = 4/h^2$ and for the other components, which are omitted here for brevity, similar equations with the obvious adaptations are used.

4. Finite Element Formulation

In the present work, a non-conforming triangular plate/shell finite element model is used, having three nodes and eight degrees of freedom per node: the displacements u_{0_i}, v_{0_i}, w_{0_i}, the slopes $(-\partial w_0/\partial y)_i$, $(\partial w_0/\partial x)_i$ and the rotations $\theta_{xi}, \theta_{yi}, \theta_{zi}$. The rotation θ_{zi} is introduced to consider a fictitious stiffness coefficient $K_{\theta Z}$ to eliminate the problem of a singular stiffness matrix for general shape structures [43]. The element local displacements, rotations and slopes, are expressed in terms of nodal variables through shape functions $\mathbf{N}_i$ given in terms of area co-ordinates L_i [43]. The displacement field can be represented in matrix form as:

$$\mathbf{u} = \mathbf{Z} \left(\sum_{i=1}^{3} \mathbf{N}_i \, \mathbf{d}_i \right) = \mathbf{Z} \, \mathbf{N} \, \mathbf{a} \quad ; \quad \mathbf{d} = \sum_{i=1}^{3} \mathbf{N}_i \, \mathbf{d}_i = \mathbf{N} \, \mathbf{a} \tag{12}$$

with

$$\mathbf{Z}=\begin{bmatrix} 1 & 0 & 0 & 0 & -z^3c_1 & 0 & -z+z^3c_1 & 0 \\ 0 & 1 & 0 & z^3c_1 & 0 & z-z^3c_1 & 0 & 0 \\ 0 & 0 & 1 & 0 & 0 & 0 & 0 & 0 \end{bmatrix} \tag{13}$$

where $\mathbf{a}$ and $\mathbf{d}_i$ are the element and nodal displacement vectors, respectively,.

The membrane, bending and shear strains, as well the higher order bending and shear strains can be represented by:

$$\boldsymbol{\varepsilon}_m=\mathbf{B}^m\,\mathbf{a}\;\;;\;\;\boldsymbol{\varepsilon}_b=z\,\mathbf{B}^b\,\mathbf{a}\;\;;\;\;\boldsymbol{\varepsilon}_s=\mathbf{B}^s\,\mathbf{a}\;\;;\;\;\boldsymbol{\varepsilon}_{*b}=z^3\,\mathbf{B}^{*b}\,\mathbf{a}\;\;;\;\;\boldsymbol{\varepsilon}_{*s}=z^2\,\mathbf{B}^{*s}\,\mathbf{a} \tag{14}$$

where the $\mathbf{B}^m$, $\mathbf{B}^b$, $\mathbf{B}^{*b}$, $\mathbf{B}^s$ and $\mathbf{B}^{*s}$ are the components of the strain-displacement matrix $\mathbf{B}$, which are given explicitly in [44].

The Virtual Work Principle equation, applied to a finite element, can be written in the form:

$$\sum_{k=1}^{N}\left\{\int_{{}^tA^e}\int_{h_{k-1}}^{k_k}\delta\,{}_t\varepsilon_k^L\,Q_k\,{}_t\varepsilon_k^L\,dz\,{}^tdA^e+\int_{{}^tA^e}\int_{h_{k-1}}^{k_k}\delta\,{}_t\varepsilon_k^{NL}\,{}^t\sigma_k^L\,dz\,{}^tdA^e\right\}=$$
$$ {}^{t+\Delta t}_t\Re^e-\sum_{k=1}^{N}\int_{{}^tA^e}\int_{h_{k-1}}^{k_k}\delta\,{}_t\varepsilon_k^L\,{}^t\sigma_k^L\,dz\,{}^tdA^e \tag{15}$$

where $\Re^e$ is the external virtual work. From this equation, we obtain the element linear stiffness matrix $\mathbf{K}_L^e$, the element geometric stiffness matrix $\mathbf{K}_\sigma^e$, as well as element external load vector $\mathbf{F}_{ext}^e$ and the element internal force vector $\mathbf{F}_{int}^e$, and are defined as follows:

$$\mathbf{K}_L^e=\int_{A^e}\mathbf{B}^T\left(\sum_{k=1}^{N}\hat{\mathbf{D}}_k\right)\mathbf{B}\,dA^e \tag{16a}$$

$$\mathbf{K}_\sigma^e=\int_{{}^tA^e}\mathbf{G}^T\left(\sum_{k=1}^{N}\hat{\boldsymbol{\tau}}_k\right)\mathbf{G}\;{}^tdA^e \tag{16b}$$

$$\mathbf{F}_{int}^e=\int_{{}^tA^e}\mathbf{B}^T\left(\sum_{k=1}^{N}\hat{\mathbf{D}}_k\right)\,{}_t\boldsymbol{\varepsilon}_k^0\;{}^tdA^e \tag{16c}$$

These matrices and vectors are initially computed in the local coordinate system attached to the element and then the standard local to global transformations are performed [43]. By adding the contributions of all the elements in the domain, the system equilibrium equations are obtained as:

$${}^{t+\Delta t}_{t+\Delta t}\left(\mathbf{K}_L+\mathbf{K}_\sigma\right)^{i-1}\left(\Delta\mathbf{q}\right)^i={}^{t+\Delta t}\mathbf{F}_{ext}-{}^{t+\Delta t}_{t+\Delta t}\left(\mathbf{F}_{int}\right)^{i-1} \tag{17}$$

where $\mathbf{K}_L$, $\mathbf{K}_\sigma$, $\mathbf{F}_{ext}$, $\mathbf{F}_{int}$, $\Delta\mathbf{q}$, are the system stiffness matrix, geometric stiffness matrix, external load vector, internal load vector, and incremental displacement vector in global coordinate system, respectively

Using the Newton-Raphson incremental-iterative method [45], the incremental equilibrium path is obtained. For linear buckling analysis, we make use of only one load increment, and equation (41) takes the following form:

$$\left(\mathbf{K}_L + \mathbf{K}_\sigma\right)\mathbf{q} = \mathbf{F}_{ext} \tag{18}$$

The instability takes place when the determinant of the tangential matrix is zero. The corresponding eigenvalue problem can be solved, obtaining the critical load as follows

$$\left(\mathbf{K}_L + \lambda_{cr}\,\mathbf{K}_\sigma\right)\mathbf{v} = 0 \;\; ; \;\; {}^{cr}\mathbf{F}_{ext} = \lambda_{cr}\,\mathbf{F}_{ext} \tag{19}$$

The dynamic equation is obtained from the Hamilton's principle. We can write:

$$\int_{t_1}^{t_2}\left[\sum_{k=1}^{N}\left(\int_{A^e}\int_{h_{k-1}}^{h_k}\delta\mathbf{a}^T\,\mathbf{B}^T\mathbf{Q}\,\mathbf{B}\;\mathbf{a}\,dz\,dA^e - \int_{\mathbf{A}}\mathbf{N}^T\,\delta\dot{\mathbf{a}}^T\rho_k\left(\int_{h_{k-1}}^{h_k}\mathbf{Z}^T\mathbf{Z}\,dz\right)\mathbf{N}\,\dot{\mathbf{a}}\,dA^e\right)\right]dt = 0 \tag{20}$$

where **N** is the shape functions matrix. For free vibrations we have:

$$\left(\mathbf{K}_L - \omega^2\,\mathbf{M}\right)\mathbf{v} = 0 \quad . \tag{21}$$

The corresponding eigenvalue problem can be solved and the natural frequencies are obtained. The mass matrix **M** in equation (21) is defined by

$$\mathbf{M} = \int_A \mathbf{N}^T\sum_{k=1}^{N}\rho_k\left(\int_{h_{k-1}}^{h_k}\mathbf{Z}^T\mathbf{Z}\;dz\right)\;\mathbf{N}\;\;dA^e\;. \tag{22}$$

5. SENSITIVITY ANALYSIS IN P-FGM STRUCTURES

From the equations (2) and (3), the material properties (H) of each layer k of an FGM, can be written as a function of volume fraction V_c^k

$$H^k = V_c^k\left(H_c - H_m\right) + H_m \tag{23}$$

Differentiating in order to a general design variable b, we can write

$$\frac{dH^k}{db} = \frac{dV_c^k}{db}\left(H_c - H_m\right) = \frac{d}{db}\left(0.5 + \frac{1}{h}\bar{z}_k\right)^p\left(H_c - H_m\right) \tag{24}$$

For design variable p-index, we have

$$\frac{dH^k}{dp}=\left(0.5+\frac{1}{h}\bar{z}_k\right)^p \ln\left(0.5+\frac{1}{h}\bar{z}_k\right)\left(H_c-H_m\right) \quad ; \quad H^k=E^k,\rho^k \tag{25}$$

and for design variable thickness h, we have

$$\frac{dH^k}{dh}=-p\left(0.5+\frac{1}{h}\bar{z}_k\right)^{p-1}\left(\frac{\bar{z}_k}{h^2}\right)\left(H_c-H_m\right) \quad ; \quad H^k=E^k,\rho^k \quad . \tag{26}$$

5.1 Linear analysis

Differentiating the linear analysis equation, $\mathbf{K}_L\,\mathbf{q}=\mathbf{F}_{ext}$, we get

$$\frac{dq}{db}=-\mathbf{K}_L^{-1}\left(\frac{\partial \mathbf{K}_L}{\partial b}\mathbf{q}\right) \tag{27}$$

The element stiffness matrix given by equation (16a) can also be written in the form:

$$\mathbf{K}_L=\int_A \mathbf{B}^T \sum_{k=1}^{N} \mathbf{Q}_k \frac{z_{k+1}^n-z_k^n}{n}\mathbf{B}\;dA \tag{28}$$

and its derivatives come as follows:

$$\frac{\partial \mathbf{K}_L}{\partial p}=\int_A \mathbf{B}^T \sum_{k=1}^{N} \frac{\partial \mathbf{Q}_k}{\partial p}\frac{z_{k+1}^n-z_k^n}{n}\mathbf{B}\,dA \;, \quad n = 0,1,2,3,4,5,7 \tag{29a}$$

$$\frac{\partial \mathbf{K}_L}{\partial h}=\int_A \mathbf{B}^T \sum_{k=1}^{N} \frac{\partial \mathbf{Q}_k}{\partial h}\frac{z_{k+1}^n-z_k^n}{n}\mathbf{B}\,dA+\int_A \mathbf{B}^T\mathbf{Q}_k\frac{\partial}{\partial h}\left(\frac{z_{k+1}^n-z_k^n}{n}\right)\mathbf{B}\,dA \tag{29b}$$

with $\frac{\partial \mathbf{Q}_k}{\partial b}=\frac{\partial E_k}{\partial b}\mathbf{c}$, from equation (6), and $\frac{\partial E_k}{\partial b}$ is given by equations (25) and (26).

5.2 Nonlinear analysis

The sensitivities of the displacement vector and limit load, are obtained as shown in Moita et al. [37] resulting in

$$\frac{d\mathbf{q}}{db}=-\mathbf{K}_T^{-1}\left(\mu\frac{d\mathbf{F}_{ext}}{db}-\frac{\partial \mathbf{F}_{int}}{\partial b}\right) \tag{30}$$

$$\frac{d\mu^b}{db}=\frac{\mathbf{v}^T\left(\frac{\partial \mathbf{F}_{int}^b}{\partial b}-\mu^b\frac{d\mathbf{F}_{ext}^0}{db}\right)}{\mathbf{v}^T\,\mathbf{F}_{ext}^0} \tag{31}$$

where the derivative of the internal force vector is given by

$$\frac{\partial \mathbf{F}_{\text{int}}}{\partial b} = \int_A \mathbf{B}^T \frac{\partial \hat{\mathbf{D}}}{\partial b}\, {}_t\boldsymbol{\varepsilon}_L^{0\ t} dA = \int_A \mathbf{B}^T \sum_{k=1}^{N} \frac{\partial}{\partial b}\left(\mathbf{Q}_k \frac{z_{k+1}^n - z_k^n}{n} \right) {}_t\boldsymbol{\varepsilon}_L^{0\ t} dA . \tag{32}$$

5.3 Fundamental frequency

From the eigenvalue problem in equation (21), we obtain, after development, the sensitivity of the fundamental frequency, as well as the sensitivity of frequency constraint defined by $\overline{\psi} = 1 - \omega/\omega_0 \le 0$, as follows

$$\frac{d\omega}{db} = \frac{1}{2\omega} \mathbf{v}^T \left(\frac{\partial \mathbf{K}_L}{\partial b} - \omega^2 \frac{\partial \mathbf{M}}{\partial b} \right) \mathbf{v} \tag{33}$$

$$\frac{d\overline{\psi}}{db} = -\frac{1}{2\omega\,\omega_0} \mathbf{v}^T \left(\frac{\partial \mathbf{K}_L}{\partial b} - \omega^2 \frac{\partial \mathbf{M}}{\partial b} \right) \mathbf{v} \tag{34}$$

where the derivatives of element mass matrix, equation (22), are given by:

$$\frac{\partial \mathbf{M}}{\partial p} = \int_A \mathbf{N}^T \left(\sum_{k=1}^{N} \int_{h_k}^{h_{k+1}} \mathbf{Z}^T\, \mathbf{Z}\, dz \frac{\partial \rho_k}{\partial p} \right) \mathbf{N}\, dA \tag{35a}$$

$$\frac{\partial \mathbf{M}}{\partial h} = \int_A \mathbf{N}^T \left(\sum_{k=1}^{N} \int_{h_k}^{h_{k+1}} \mathbf{Z}^T\, \mathbf{Z}\, dz \frac{\partial \rho_k}{\partial h} \right) \mathbf{N}\, dA + \int_A \mathbf{N}^T \sum_{k=1}^{N} \rho_k \int_{h_k}^{h_{k+1}} \frac{\partial (\mathbf{Z}^T\, \mathbf{Z})}{\partial h} dz\, \mathbf{N}\, dA \tag{35b}$$

5.4 Critical load

From the equation (19), we obtain, after development, the sensitivity of critical load parameter λ_{cr} and of the critical load constraint defined by $\overline{\psi} = \lambda_{cr}/\lambda_{cr0} - 1 \le 0$, as follows

$$\frac{d\lambda_{cr}}{db} = \mathbf{v}^T \left(\frac{\partial \mathbf{K}_L}{\partial b_i} - \lambda_{cr} \frac{\partial \mathbf{K}_\sigma}{\partial b} \right) \mathbf{v} \tag{36}$$

$$\frac{d\overline{\psi}}{db} = \frac{1}{\lambda_{cr0}} \mathbf{v}^T \left(\frac{\partial \mathbf{K}_L}{\partial b} - \lambda_{cr} \frac{\partial \mathbf{K}_\sigma}{\partial b} \right) \mathbf{v} = 0 \tag{37}$$

where

$$\frac{\partial \mathbf{K}_\sigma}{\partial b} = \int_A \mathbf{G}^T \frac{\partial \hat{\boldsymbol{\tau}}}{\partial b} \mathbf{G}\ dA \tag{38}$$

5.6 Effective stress constraint

Considering the Huber-Mises criterion, for the case of an isotropic material, the effective stress $\overline{\sigma}$ is given by

$$\overline{\sigma}_{\mathrm{k}}=\left[\left({}^{\mathrm{t}}\sigma_{11}\right)_{\mathrm{k}}^{2}+\left({}^{\mathrm{t}}\sigma_{22}\right)_{\mathrm{k}}^{2}-\left({}^{\mathrm{t}}\sigma_{11}\ {}^{\mathrm{t}}\sigma_{22}\right)_{\mathrm{k}}+3\left({}^{\mathrm{t}}\sigma_{12}\right)_{\mathrm{k}}^{2}+3\left({}^{\mathrm{t}}\sigma_{13}\right)_{\mathrm{k}}^{2}+3\left({}^{\mathrm{t}}\sigma_{23}\right)_{\mathrm{k}}^{2}\right]^{1/2} \tag{39}$$

The effective stress constraint, for the present model, is defined as follows

$$\overline{\psi}=\frac{\overline{\sigma}_{\mathrm{k}}}{\left(\sigma_{\mathrm{Y}}\right)_{\mathrm{k}}}=\frac{\left[{}^{\mathrm{t}}\left(\sigma_{11}\right)_{\mathrm{k}}^{2}+\left({}^{\mathrm{t}}\sigma_{22}\right)_{\mathrm{k}}^{2}-\left({}^{\mathrm{t}}\sigma_{11}\ {}^{\mathrm{t}}\sigma_{22}\right)_{\mathrm{k}}+3\left({}^{\mathrm{t}}\sigma_{12}\right)_{\mathrm{k}}^{2}+3\left({}^{\mathrm{t}}\sigma_{13}\right)_{\mathrm{k}}^{2}+3\left({}^{\mathrm{t}}\sigma_{23}\right)_{\mathrm{k}}^{2}\right]^{1/2}}{\left(\sigma_{\mathrm{Y}}\right)_{\mathrm{k}}} \tag{40}$$

where

$${}^{\mathrm{t}}\boldsymbol{\sigma}_{\mathrm{k}}^{\mathrm{m,b,*b}}=\mathbf{Q}_{\mathrm{k}}\ {}_{\mathrm{t}}\boldsymbol{\varepsilon}_{\mathrm{k}}=\mathbf{Q}_{\mathrm{k}}\left(\mathbf{B}^{\mathrm{m}}+\overline{\mathrm{z}}\,\mathbf{B}^{\mathrm{b}}+\overline{\mathrm{z}}^{\mathbf{3}}\,\mathrm{B}^{*\mathrm{b}}\right)\mathbf{a}$$

$${}^{\mathrm{t}}\boldsymbol{\sigma}_{\mathrm{k}}^{\mathrm{s}}=\mathbf{Q}_{\mathrm{k}}\ {}_{\mathrm{t}}\boldsymbol{\varepsilon}_{\mathrm{k}}=\mathbf{Q}_{\mathrm{k}}\left(\mathbf{B}^{\mathrm{s}}+\overline{\mathrm{z}}^{2}\,\mathbf{B}^{*\mathrm{s}}\right)\mathbf{a} \tag{41}$$

and t means current time (at the end of the final increment) and σ_{Y}, for each virtual layer is obtained as follows [2,46]:

$$\sigma_{Y}^{k}=\sigma_{Ym}\left(\mathrm{V}_{m}+\frac{q+\mathrm{E}_{m}}{q+\mathrm{E}_{c}}\frac{\mathrm{E}_{c}}{\mathrm{E}_{m}}\mathrm{V}_{c}\right) \tag{42}$$

where q is the stress-strain transfer parameter given in [2,46] and the ratio q/Ec is taken as 0.60-0.80, based on the micro-indentation experiments.

The sensitivity of effective stress constraint is then given by:

$$\left(\frac{\mathrm{d}\overline{\psi}}{\mathrm{db}}\right)_{\mathrm{k}}=\left(\frac{\partial\overline{\psi}}{\partial\mathrm{b}}\right)_{\mathrm{k}}+\left(\frac{\partial\overline{\psi}}{\partial\mathbf{a}}\right)_{\mathrm{k}}\left(\frac{\mathrm{d}\mathbf{a}}{\mathrm{db}}\right) \tag{43}$$

where the derivatives of $\left(\partial\overline{\psi}/\partial\mathrm{b}\right)_{\mathrm{k}}$ and $\left(\partial\overline{\psi}/\partial\mathrm{a}\right)_{\mathrm{k}}$ are given explicitly in the Appendix.

6. Optimization

In the present work the objective of optimization is to find the design variables **b** that minimize or maximize an objective function, subject to certain constraints:

$$\begin{aligned} &\textit{min}\ \ \varphi\left(\mathbf{q},\mathbf{b}\right)\ \ \text{or}\ \ \textit{max}\ \ \varphi\left(\mathbf{q},\mathbf{b}\right)\\ &\textit{subject to}\qquad \overline{\psi}^{i}\left(\mathbf{q},\mathbf{b}\right)\le 0\,,\ i=0,1,..\mathrm{n}\\ &\qquad\qquad \mathbf{b}^{l}\le\mathbf{b}\le\mathbf{b}^{u} \end{aligned} \tag{44}$$

where b^l and b^u are the lower and upper limits of the design variables, and **q** is the global displacements vector.
The optimization problem is solved by using a gradient-based algorithm FAIPA, the Feasible Arc Interior Point Algorithm, developed by Herskovits et al. [47-48].

7. Applications

7.1 Optimization of a simply supported square FGM plate – Linear Analysis

First, we consider the optimization problem of a square simply supported FGM plate with constituents Silicon Nitride, having the following mechanical properties: E_c = 348.430 GPa, ρ_c = 2370 kg/m3, ν_c = 0.24 and Stainless Steel, having the properties: E_m = 201.040 GPa, ρ_m = 8166 kg/m^3, ν_m = 0.3262. The length of the plate sides is a = 0.5 m and the thickness of the plate is h = 0.035 m. In this numerical example, we compare the optimization results obtained with the present model with those published by Franco Correia et al. [36] for two different optimization problems. In the initial design the plate has a p-index of 1.0. The design variables of the optimization problem are the p-index and the thickness of the plate. In the first optimization problem, the design objective is the maximization of the fundamental natural frequency. In the second optimization problem, the design objective is the minimization of the plate overall mass. In both cases, a constraint is imposed on the fundamental natural frequency: $3000 \leq \omega \leq 8000$ (rad/s).
The optimization results are compared in Table 1, and a very good agreement is achieved, with the alternative solutions of Franco Correia et al [36] obtained by using a derivative free method, the Global and Local Optimization with Direct Search algorithm (GLODS). Although both models use higher-order shear deformation theories, the different finite element geometries and mesh sizes do justify the small differences obtained.

Table 1. Comparison of optimization solutions

Solutions	Objective functions		Design variables	
	Fundamental natural frequency (rad/s)	Mass (kg)	Index p	Thickness (mm)
Initial design				
Present model	5855.04	46.09	1.0	35
Correia et al. [36]	5760.81	46.10	1.0	35
1st optimization problem				
Present model	8000.00	103.74	3.8	59.5
Correia et al. [36]	8000.00	101.20	3.4	59.1
2nd optimization problem				
Present model	5790.00	21.37	0.2	25.7
Correia et al. [36]	5705.85	21.50	0.2	25.8

7.2 Optimization of a simply supported square FGM plate – Nonlinear Analysis

The optimization of a simply supported square FGM plate made of Zirconia and Stainless Steel, subjected to transverse uniform load and having a side-to-thickness ratio of a/h=60 (a=0.6 m, h=0.01m) is now considered with a nonlinear analysis. Zirconia has the following mechanical properties: E_c = 151 GPa, ρ_c = 3000 kg/m^3 and ν_c =0.3. Stainless Steel has the following mechanical properties: E_m = 207.7877 GPa, ρ_m= 8166 kg/m^3, ν_m = 0.3177.
The analytical sensitivities accuracy comparison is performed for this example, with a p-index p=5.0. By considering first a static nonlinear analysis, the sensitivities of the central displacement w_c and of the effective stress $\bar{\sigma}$ were obtained at the end of the incremental iterative process with F =125 kN/m^2. In a free-vibration analysis, the sensitivity of the fundamental frequency was also calculated. In Table 2, the results obtained with the present method of analytical sensitivities are compared with those calculated by Global Finite Differences (GFD) and a good agreement can be observed. The results obtained for mass, centre displacement and fundamental frequency as a function of the power law exponent p (varying between 0.1 and 10.0) are shown in Figure 2. From the Figure 2 it can be observed that the minimum mass and the maximum fundamental frequency are obtained when p=0.1, but the minimum centre displacement is obtained for p=10.

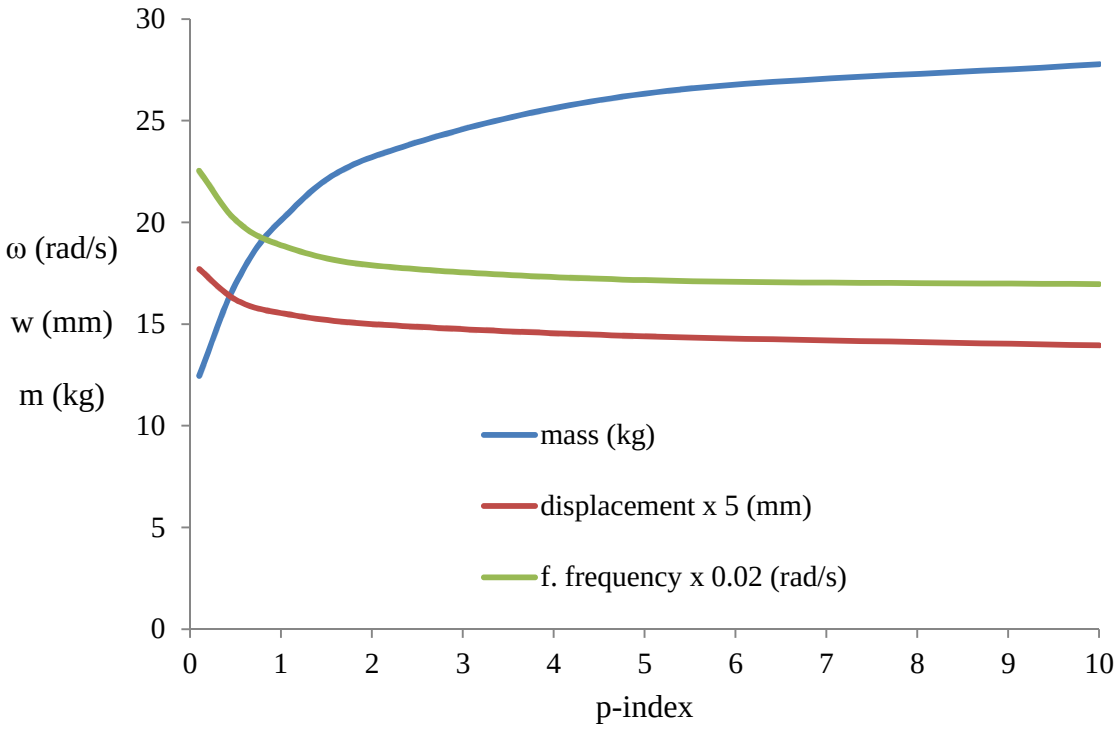

Figure 2. Variation of mass, displacement and frequency versus p-index

Table 2. Sensitivities for the simply supported FGM plate. Comparison between analytical and Global Finite Differences (GFD).

Sensitivity	GFD		Analytical	
	Variable p	Variable h	Variable p	Variable h
Displacement w_c	$-2.91\text{x}10^{-5}$	$-9.01\text{x}10^{-1}$	$-2.74\text{x}10^{-5}$	$-9.30\text{x}10^{-1}$
$\overline{\psi}=\frac{\overline{\sigma}_k}{(\sigma_Y)_k}$	$-1.68\text{x}10^{-3}$	-68.71	$-1.59\text{x}10^{-3}$	-70.10
Fund. Frequency ω	-4.74	84878.7	-4.77	82724.6

The initial design of the plate is taken with an exponent p = 1.0 which corresponds to a mass of m = 20.1 kg. The centre displacement and effective stress in nonlinear behaviour and the fundamental frequency were evaluated for the initial design. For the load level F = 125 kN/m^2, corresponding to three increments, the centre displacement and effective stress were w_c=3.73 mm and $\overline{\sigma}=154.0\,\text{MPa}$, respectively. The stresses have been evaluated at the mid-surface of the considered 20 virtual layers in which the panel has been discretized through the thickness and it was considered $\sigma_{Y\,\text{Stainless Steel}}$ = 40 MPa and q = 120 GPa. For the initial design, the fundamental frequency of the plate obtained by solving the eigenvalue problem, was ω = 948.25 rad/s.

The optimization problem consisted in searching the power law exponent p that minimize the mass of the plate considering the following constraints: maximum center displacement $w_{max} \le 4.0\,\text{mm}$; maximum effective stress $\overline{\sigma} \le \sigma_{Y_{FGM}}$; and minimum fundamental frequency with the constraint $\omega \ge 948.2\,\text{rad/s}$. The optimal design was achieved for p = 0.28 with corresponding mass m = 14.86 kg. The optimization results are presented in Table 3.

Table 3. Optimal design results for the simply supported FGM plate.

Initial design	Variable p	m (kg)	w_c (mm)	$\overline{\sigma}$ (MPa)	ω (rad/s)
	1.0	20.10	3.73	154.0	948.25
Optimal design			Constraint $w_c \le 4.0$	Constraint $\overline{\sigma} \le \sigma_Y$	Constraint $\omega \ge 948.2$
	0.28	14.86	4.00 (1)	155.3	1060.0

(1) active constraint

7.3 Optimization of a hinged functionally graded cylindrical panel

The optimization problem of a FGM cylindrical shell panel as represented in Figure 3 is now considered. The shell has the straight sides hinged and the curved sides free. The geometry is defined by: R= 2.54 m, L = 0.508 m, the subtended angle is 2θ=0.2 rad, h=0.0126 m. The panel has been modelled by using an 8x8 finite element mesh. The constituents are Zirconia for the ceramic and Aluminium for the metal with the following mechanical properties: E_c =

151 GPa, ρ_c = 3000 kg/m^3, E_m = 70 GPa, ρ_m = 2707 kg/m^3, $\nu_c = \nu_m$ = 0.3. Considering a power law exponent p = 5 the cylindrical panel has a mass of m = 8.96 kg.

The panel is subjected to a centre point reference load F_0 = 60 kN. In geometrically nonlinear analysis using an incremental-iterative process, a centre displacement w_c=7.96 mm was obtained with 6 increments (F=51.0 kN). In a first optimization level the goal was to minimize the centre displacement considering the power law exponent p as design variable. It was considered that the p-index was restricted to the range of: 0.2 < p < 10. In a second optimization level the design variable was the thickness of the panel and the objective function was the minimization of the mass of the structure. Two constraints were considered: the maximum centre displacement of $w_{max} \leq 4.0$ mm; and a maximum effective stress (at the metal surface) of $\bar{\sigma} \leq \sigma_{Y_{FGM}}$, considering $\sigma_{Y\,\text{Aluminium}} = 25$ MPa and $q = 120$ GPa. In order to consider these constraints a geometric (G) and a materially (M) nonlinear analysis were required. Table 4 presents the optimization results with the values of the constraints, objective functions and design variables for the initial and optimal designs.

For the second level of the optimization, considering the panel divided into 4 groups of finite elements, as shown in Figure 4 (symmetry considered), the optimal design of the shell can be obtained for the values of the design variables given in Table 5, corresponding to the mass m = 8.68 kg. Figure 5 shows the load-displacement paths for the initial design of the structure and for the optimal one.

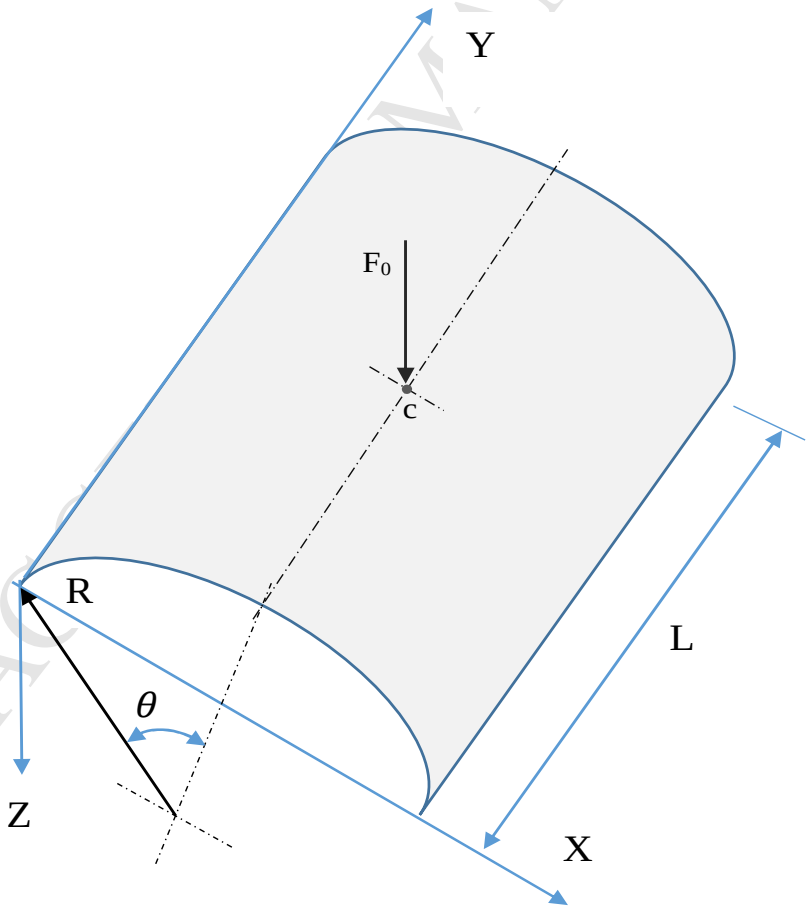

Figure 3. Cylindrical FGM panel.
(Upper face - ceramic: z = - h/2; lower face - metal: z = + h/2).

Table 4. Optimal design results for the hinged-free FGM cylindrical panel.

Cylindrical Panel	Initial	Optimal
1st level of optimization		
Variable p	5.0	0.2
Mass (kg)	8.96	9.60
Objective: *min*(w_c) (mm)	11.60	3.40
2nd level of optimization		
Variable h (mm)	12.60	12.0
Constraint: w = 4.0 (mm)	3.40	4.0
Constraint: $\bar{\sigma}$ (MPa)	285.0	284.0
Objective: *min*(m) (kg)	9.60	9.15

Table 5. Optimal design results for the hinged-free FGM cylindrical panel using 4 groups of finite elements

	2nd level of optimization	
	Initial	Optimal
Objective: *min*(m) (kg)	9.60	8.68
Constraint: w ≤ 4.0 (mm)	3.40	4.00
Constraint: $\bar{\sigma}$ ≤ 285.0 (MPa)		272.13
Thickness h_i (mm)	12.60	
Element group number		
1		9.40
2		11.16
3		12.34
4		12.68

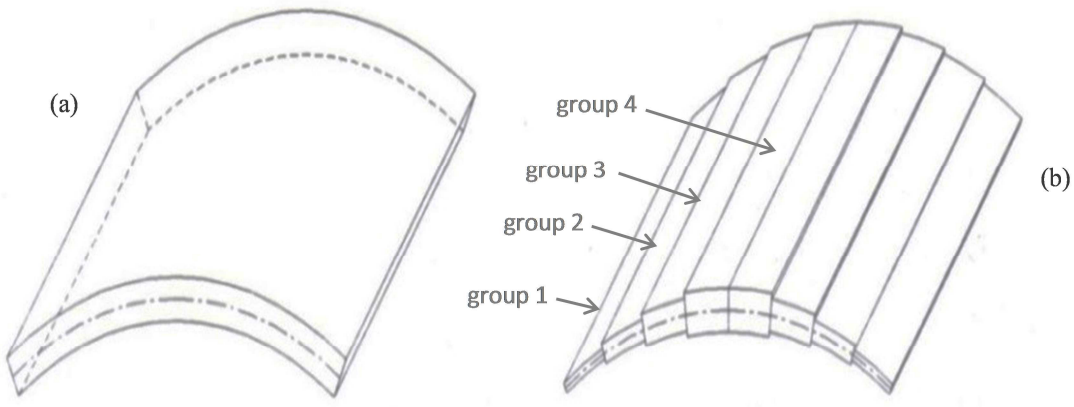

Figure 4. Initial (a) and optimal (b) thickness distribution in the panel. Definition of the 4 groups of elements used in the optimization process.

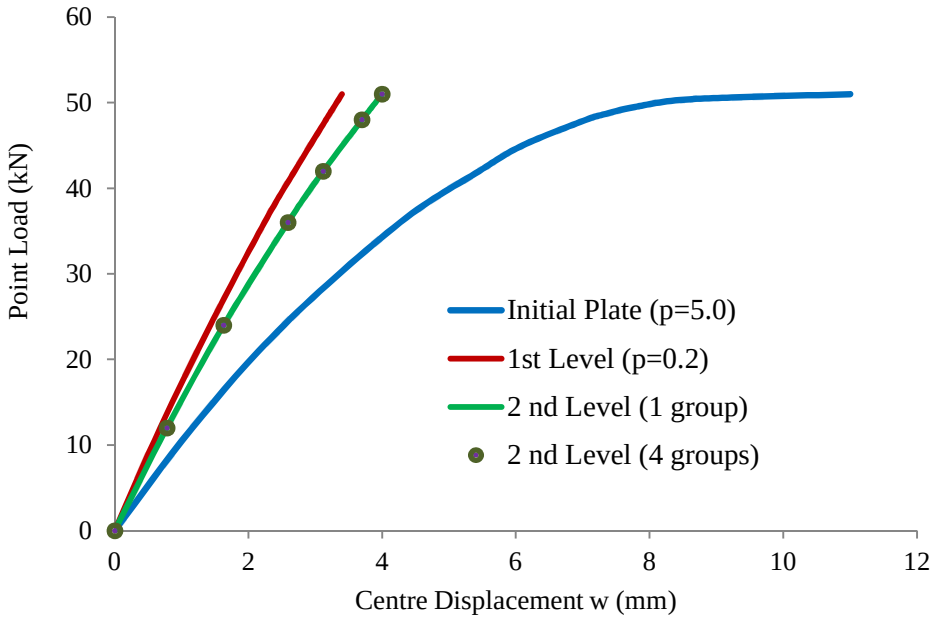

Figure 5. Load-displacements paths considering geometric and materially nonlinear behaviour

7.4 Optimization of a simply-supported functionally graded cylindrical panel

An FGM cylindrical shell panel with all sides simply supported is now considered. The geometry is defined by: R= 20.0 m, L = 2.0 m and subtended angle 2θ=0.1 rad, thickness h = 0.02 m. A 10×10 finite element mesh has been used. The constituents are Alumina as ceramic and Aluminium as metal. The material properties of both constituents are, respectively: E_c=380 GPa, ρ_c=3000 kg/m^3, ν_c =0.3, E_m=70 GPa, ρ_m=2707 kg/m^3 and ν_m=0.3. The initial panel with a p-index p=5.0 and corresponding mass m=220.42 kg, is subjected to a centre point reference load of F_0=60 kN. In a geometrically nonlinear analysis using an incremental-iterative process, a centre displacement of w_c=12.9 mm and an effective stress of $\bar{\sigma} = 117.0$ MPa are obtained with 3 increments for the load level F = 30 kN. The fundamental frequency obtained for this initial plate design was $\omega = 262.5$ rad/s.

The optimization consists in searching the power law exponent p and thickness h, taken jointly, that minimizes the mass of panel, subjected to three constraints: the maximum centre displacement constraint $w_{max} \le 4.5$ mm, the effective stress constraint $\bar{\sigma} \le \sigma_Y$, and the minimum fundamental frequency $\omega_{min} \ge 400.0$ rad/s. The stresses have been evaluated at the mid-surface of the considered 20 virtual layers in which the panel has been discretized through the thickness, considering $\sigma_{Y\,\text{Aluminium}}$ = 25 MPa and q = 250 GPa. Table 6 describes the results of the optimization process.

Table 6. Optimal design results for the simply supported FGM cylindrical panel

Cylindrical panel	Initial	Optimal
Variable p	5.0	0.1
Thickness h (mm)	20.0	18.33
Objective: *min*(m) (kg)	220.4	218.0
Constraint: w_c (mm)$\leq$4.5	12.9	4.5
Constraint: ω (rad/s)$\geq$400.0	262.5	405.6
Constraint: $\bar{\sigma}$ (MPa)$\leq \sigma_Y$	117.0	86.4

7.5 Snap-Through optimization of a hinged functionally graded cylindrical panel

In this example the FGM cylindrical shell has the straight sides simply-supported (hinged) and the curved sides free, as in section 7.3. The geometry is defined by: R= 2.54 m, L = 0.508 m and subtended angle 2θ=0.2 rad, h=0.0126 m, and it is modelled by an 8x8 finite element mesh. The constituents are Zirconia as ceramic and Aluminium as metal with the following properties: E_c = 151 GPa, ρ_c = 3000 kg/m^3, ν_c =0.3, E_m=70 GPa, ρ_m=2707 kg/m^3, ν_m = 0.3.
The initial panel with a p-index p=0.1 is subjected to a centre point reference load F_0=60 kN. For this specific situation of geometry and boundary conditions, snap-through occurs. Thus we can try to get a new cylindrical panel with the same boundary conditions, geometry, applied load and mass, but where the snap-through phenomena does not occur. To do so, the panel is divided into 16 groups of elements, as shown in Figure 6, to allow for some possibility of variation of thickness over the panel domain. The optimization consists in the maximization of the limit load under a mass constraint (equal to the mass of the initial panel), and the design variables – thicknesses h_i for each group - varying between the boundary values of 5 and 35 mm.
In this type of optimization it is observed that some restarts need to be done. Since the maximization of objective function – limit load – allows for some different sets of thickness distribution that fulfil the requirement of avoiding the snap-through effect, different sets of thickness distribution over the panel have been considered. Table 7 shows two possible sets of thickness distribution, where for panel A the final mass is 0.16% less than the initial mass. In Figure 7 the load-displacement paths are presented for the initial and for those two possible solutions for the optimal panel.

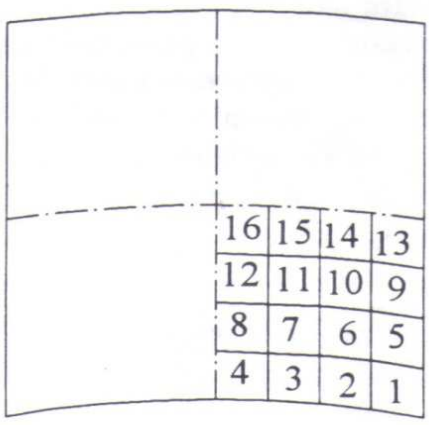

Figure 6. Definition of the 16 group numbers

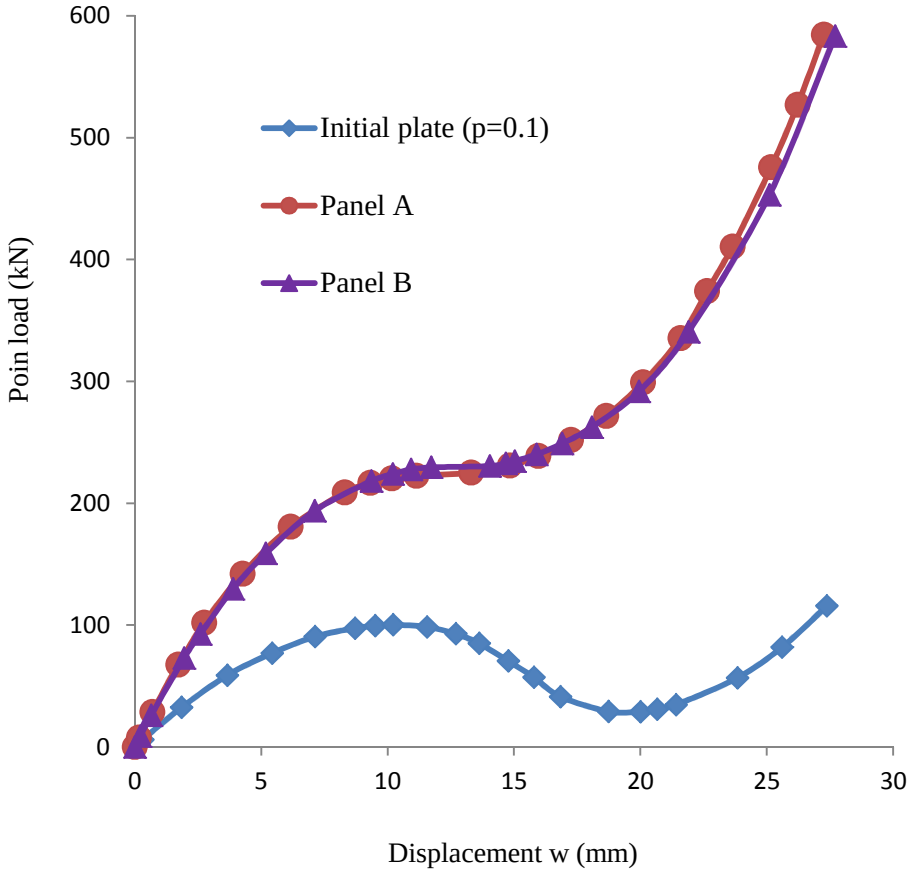

Figure 7. Load-displacement paths for initial and optimal panel configurations

Table 7. Thickness distribution

Element group number	Initial thicknesses[(1)]	Thickness distributions (mm)	
		Panel A	Panel B
1	12.6	5.0	5.4
2		5.0	5.4
3		5.0	5.4
4		5.1	6.3
5		6.4	6.3
6		6.4	6.3
7		6.2	6.3
8		6.0	7.2
9		11.0	7.2
10		11.0	7.2
11		10.6	7.2
12		10.4	31.3
13		19.6	31.3
14		28.2	31.3
15		32.0	31.3
16		33.4	31.3

[(1)] Equal thickness for all elements in the initial design

8. CONCLUSIONS

In the present work, a high order shear deformation theory was applied to develop a discrete model for the structural and sensitivity analyses allowing for the material distribution and sizing optimization of functionally graded material structures. The formulation accounts for geometric and material nonlinear behaviour, free vibrations and linear buckling analyses, and their analytical sensitivities aimed to be used with the gradient-based optimization algorithm. The p-index of the power–law material distribution and the thickness were considered as design variables.

Several optimization solutions obtained by using the gradient based method FAIPA, Feasible Arc Interior Point Algorithm, for simple plate and shell FGM structures were presented for benchmarking purposes.

The comparison of the present gradient-based optimization results were in good agreement with alternative values obtained by a derivative-free algorithm for two simple optimization problems of FGM plates with linear behaviour.

The accuracy and efficiency of the analytical sensitivities with respect to p-index and the thickness of the plate-shell FGM structures have been validated by comparison with the sensitivities calculated by global finite differences.

The optimization process performed with the gradient-based algorithm FAIPA, has showed good efficiency and proved to be a good numerical tool to obtain the optimal design of functionally graded plate and shell structures either in linear analysis as in geometric and materially nonlinear analysis.

ACKNOWLEDGEMENTS

The authors dedicate this work in honor of Professors David Hui and Luciano Feo by successfully organizing the 25th Annual International Conference on Composite and Nano Engineering (ICCE), in Rome, Italy, in July 16-22, 2017.

The fourth co-author thanks the professional recognition received by his participation on the First ICCE, in New Orleans, USA, in 1994.

This work was supported by FCT, Fundação para a Ciência e Tecnologia, through IDMEC, under LAETA, project UID/EMS/50022/2013, and also CNPq, CAPES and FAPERJ, from Brazil.

REFERENCES

1. Koizumi M, The concept of FGM Ceram. Trans. Funct. Grad. Mater. 1993; 34:3–10.
2. Moita JS, Araújo AL, Mota Soares CM, Mota Soares CA, Herskovits, J. Material and geometric nonlinear analysis of functionally graded plate-shell type structures. Applied Composite Materials, 2016.
3. Moita JS, Araújo AL, Mota Soares CM, Herskovits J, Finite element model for nonlinear analysis of functionally graded plate-shell structures. Proceedings of the XXXVI Iberian Latin-American Congress on Computational Methods in Engineering, Ney Augusto Dumont (Editor), ABMEC, Rio de Janeiro, Brazil, November 2015. p. 22-25.
4. Reddy JN, Arciniega RA, Free vibration analysis of functionally graded plates. In:

Analysis and Design of Plated Structures: Dynamics. Woodhead Publishing, Cambridge, UK, 2006.
5. Arciniega RA, Reddy JN. Large deformation analysis of functionally graded shells. International Journal of Solids and Structures 2007; 44: 2036–2052.
6. Kim KD, Lomboy GR, Han SC. Geometrically nonlinear analysis of functionally graded material (FGM) plates and shells using a four-node quasi-conforming shell element. Journal of Composite Materials 2008; 42(5): 485-511.
7. Zhao Z, Liew KM. Geometrically nonlinear analysis of functionally graded shells. International Journal of Mechanical Sciences 2009; 51: 131–144.
8. Ramus I, Mohan SC. Buckling Analysis of Rectangular Functionally Graded Material Plates under Uniaxial and Biaxial Compression Load, Procedia Engineering 2014; 86: 748-757.
9. Apuzzo, A., Barretta, R., Luciano, R., Sciarra, F.M., Penna, R., Free vibrations of Bernoulli-Euler nano-beams by the stress-driven nonlocal integral model. Composites Part B 2017; 123, 105-111.
10. Apuzzo, A., Barretta, R., Luciano, R., Some analytical solutions of functionally graded Kirchhoff plates. Composites Part B 2015; 68, 266-269.
11. Barretta, R., Feo, L., Luciano, R., Sciarra, F.M., Penna, R., Functionally graded Timoshenko nanobeams: A novel nonlocal gradient formulation. Composites Part B 2016; 100, 208-219.
12. Barretta, R., Luciano, R., Analogies between Kirchhoff plates and functionally graded Saint-Venant beams under torsion. Continuum Mechanics and Thermodynamics 2015; 27, 499-505.
13. Cho, J.R., Shin, S.W., Material composition optimization for heat-resisting FGMs by artificial neural network, Composites Part A: Applied Science and Manufacturing 2004; 35 (5): 585-594.
14. Chen, B., Tong, L., Thermomechanically coupled sensitivity analysis and design optimization of functionally graded materials, Computer Methods in Applied Mechanics and Engineering 2005; 194: 1891-1911.
15. Goupee, A.J., Vel, S.S., Multi-objective optimization of functionally graded materials with temperature-dependent material properties, Materials & Design 2007; 28: 1861-1879.
16. Goupee, A.J., Vel, S.S., Two-dimensional optimization of material composition of functionally graded materials using meshless analyses and a genetic algorithm, Computer Methods in Applied Mechanics and Engineering 2006; 195: 5926-5948.
17. Vel, S.S., Pelletier, J.L., Multi-objective optimization of functionally graded thick shells for thermal loading, Composite Structures 2007; 81: 386-400.
18. Xia, Q., Wang, M.Y., Simultaneous optimization of the material properties and the topology of functionally graded structures, Computer-Aided Design, 2008, 40 (6): 660-675.
19. Na, K.S., Kim, J.H., Volume fraction optimization of functionally graded composite panels for stress reduction and critical temperature, Finite Elements in Analysis and Design 2009; 45 (11): 845-851.
20. Mozafari, H., Ayob, A., Kamali, F., Optimization of Functional Graded Plates for Buckling Load by using Imperialist Competitive Algorithm, Procedia Technology 2012; 1: 144-152.
21. Kou, X.Y., Parks, G.T., Tan, S.T., Optimal design of functionally graded materials using a procedural model and a particle swarm optimization, Computer-Aided Design 2012; 44 (4): 300-310.
22. Noh, Y.J., Kang, Y.J., Youn, S.J., Cho, J.R., Lim, O.K., Reliability-based design

optimization of volume fraction distribution in functionally graded composites, Computational Material Science 2013; 69: 435-442.
23. Vatanabe, S.L., Paulino, G.H., Silva, E.C.N., Design of functionally graded piezocomposites using topology optimization and homogenization – Toward effective energy harvesting materials, Computer Methods in Applied Mechanics and Engineering 2013; 266: 205-218.
24. Ashjari, M., Khoshravan, M.R., Mass optimization of functionally graded plate for mechanical loading in the presence of deflection and stress constraints, Composite Structures 2014; 110: 118-132.
25. Loja, M.A.R., On the use of particle swarm optimization to maximize bending stiffness of functionally graded structures, Journal of Symbolic computation 2014; 61-62: 12-30.
26. Taheri, A.H., Hassani, B., Simultaneous isogeometrical shape and material design of functionally graded structures for optimal eigenfrequencies, Computer Methods in Applied Mechanics and Engineering 2014; 277: 46-80.
27. Taheri, A.H., Hassani, B., Moghaddam, N.Z., Thermo-elastic optimization of material distribution of functionally graded structures by an isogeometrical approach, International J. f solids and Structures 2014; 51: 416-429.
28. Wang, Z.W., Zhang, Q., Xia, L.Z., Wu, J.T., Liu, P.Q., Stress analysis and parameter optimization of an FGM pressure vessel subjected to thermo-mechanical loading, Procedia Engineering 2015; 130: 374-389.
29. Shi, J.X., Shimoda, M., Interface Shape optimization of designing functionally graded sandwich structures, Composite Structures 2015; 125: 88-95.
30. Roque, C.M.C., Martins, P.A.L.S., Differential evolution for optimization of functionally graded beams, Composite Structures 2015; 133: 1191-1197.
31. Tsiatas, G.C., Charalampakis, A.E., Optimizing the natural frequencies of axially functionally graded beams and arches, Composite Structures 2017; 160: 256-266.
32. Shabana, Y.M., Elsawaf, A., Khalaf, H., Khalil, Y., Stresses minimization in functionally graded cylinders using particle swarm optimization technique, Int. J. of Pressure Vessels and Piping 2017, 154, 1-10.
33. Andrianov, I.V., Awrejcewicz, J., Diskovsky, A.A., Functionally graded rod with small concentration of inclusions: Homogenization and optimization, Int. J, of on-Linear Mechanics 2017; 91: 189-197.
34. Lieu, Q.X., Lee, J., Modeling and optimization of functionally graded plates under thermo-mechanical load using isogeometric analysis and adaptive hybrid evolutionary firefly algorithm, Composite Structures 2017; 179: 89-106.
35. Hao Li, Zhen, L., Liang, G., Walker, P., Topology optimization for functionally graded cellular composites with metamaterials by level sets, Computer Methods in Applied Mechanics and Engineering 2018; 328: 340-364.
36. Franco Correia VM, Aguilar Madeira JF, Araújo AL, Mota Soares CM. Multiobjective optimization of ceramic-metal functionally graded plates using a higher order model. Composite Structures 2018; 183: 146-160.
37. Moita JS, Barbosa JI, Mota Soares CM, Mota Soares CA. Sensitivity analysis and optimal design of geometric nonlinear laminated plates and shells. Computers and Structures 2000; 76: 407-420.
38. Bao G, Wang L. Multiple Cracking in Functionally Graded Ceramic/Metal Coatings, International Journal of Solids and Structures 1995; 32: 2853–2871.
39. Delale F, Erdogan F. The crack problem for a nonhomogeneous plane, ASME Journal of Applied Mechanics 1983; 50: 609–614.
40. Chung YL, Chi SH. The residual stress of functionally graded materials, Journal of Chinese Institute of Civil and Hydraulic Engineering 2001; 13: 1–9.

41. Chi SH, Chung YL. Cracking in Sigmoid functionally graded coating, Journal of Mechanics 2002; 18: 41–53.
42. Reddy JN. Mechanics of Laminated Composite Plates and Shells, 2 nd Edition, CRC Press, 2004.
43. O.C. Zienkiewicz, The Finite Element Method. New York, USA: McGraw-Hill, 1977.
44. Moita JS, Araújo AL, Martins PG, Mota Soares CM, Mota Soares CA. Analysis of active-passive plate structures using a simple and efficient finite element model. Mechanics of Advanced Materials and Structures 2011; 18: 159-169.
45. Bathe KJ, Ho LW. A simple and effective element for analysis of general shell structures. Computers and Structures 1981; 13: 673-681.
46. Jin, J.H., Paulino, G.H., Dodds Jr., R.H., Cohesive fracture modeling of elastic–plastic crack growth in functionally graded materials, Eng. Fract. Mechanics 2003; 70(14): 1885–1912
47. Herskovits, J.: A two-stage feasible directions algorithm for nonlinear constrained optimization. Mathematical Programming 1986; 36, 19-38.
48. Herskovits, J.: A feasible directions interior point technique for nonlinear optimization. Journal of Optimization Theory and Applications 1998; 99: 121-146.
49. Herskovits J, Mappa P, Goulart E, Mota Soares CM. Mathematical programming models and algorithms for engineering design optimization. Computer Methods in Applied Mechanics and Engineering 2005; 194: 3244-3268.

APPENDIX

Derivatives of effective stress constraint.

$$\left(\frac{\partial\overline{\psi}}{\partial b}\right)_k = \frac{1}{\sigma_Y(\overline{\sigma})^{1/2}}\left(\frac{{}^t\sigma_{11}\,\partial{}^t\sigma_{11}}{\partial b}\right)_k + \left(\frac{{}^t\sigma_{22}\,\partial{}^t\sigma_{22}}{\partial b}\right)_k - \left(\frac{1}{2}\frac{{}^t\sigma_{22}\,\partial{}^t\sigma_{11}}{\partial b}\right)_k - \left(\frac{1}{2}\frac{{}^t\sigma_{11}\,\partial{}^t\sigma_{22}}{\partial b}\right)_k + \left(\frac{3\,{}^t\sigma_{12}\,\partial{}^t\sigma_{12}}{\partial b}\right)_k + \left(\frac{3\,{}^t\sigma_{13}\,\partial{}^t\sigma_{13}}{\partial b}\right)_k + \left(\frac{3\,{}^t\sigma_{23}\,\partial{}^t\sigma_{23}}{\partial b}\right)_k \tag{45}$$

$$\left(\frac{\partial\overline{\psi}}{\partial a}\right)_k = \frac{1}{\sigma_Y(\overline{\sigma})^{1/2}}\left(\frac{{}^t\sigma_{11}\,\partial{}^t\sigma_{11}}{\partial a}\right)_k + \left(\frac{{}^t\sigma_{22}\,\partial{}^t\sigma_{22}}{\partial a}\right)_k - \left(\frac{1}{2}\frac{{}^t\sigma_{22}\,\partial{}^t\sigma_{11}}{\partial a}\right)_k - \left(\frac{1}{2}\frac{{}^t\sigma_{11}\,\partial{}^t\sigma_{22}}{\partial a}\right)_k + \left(\frac{3^t\sigma_{12}\,\partial{}^t\sigma_{12}}{\partial a}\right)_k + \left(\frac{3^t\sigma_{13}\,\partial{}^t\sigma_{13}}{\partial a}\right)_k + \left(\frac{3^t\sigma_{23}\,\partial{}^t\sigma_{23}}{\partial a}\right)_k \tag{46}$$

$$\left(\frac{\partial{}^t\sigma_I}{\partial p}\right)_k = \left(\frac{\partial\mathbf{Q}}{\partial p}\right)_k \left({}_t\boldsymbol{\varepsilon}_m^0 + \overline{z}_k\ {}_t\boldsymbol{\varepsilon}_b^0 + \overline{z}_k^3\ {}_t\boldsymbol{\varepsilon}_{*b}^0 \,\middle|\, {}_t\boldsymbol{\varepsilon}_s^0; \overline{z}_k^2\ {}_t\boldsymbol{\varepsilon}_{*s}^0\right) \qquad i=1,2,12,13,23 \tag{47}$$

$$\left(\frac{\partial{}^t\sigma_I}{\partial h}\right)_k = \left(\frac{\partial\mathbf{Q}}{\partial h}\right)_k \left({}_t\boldsymbol{\varepsilon}_m^0 + \overline{z}_k\ {}_t\boldsymbol{\varepsilon}_b^0 + \overline{z}_k^3\ {}_t\boldsymbol{\varepsilon}_{*b}^0 \,\middle|\, {}_t\boldsymbol{\varepsilon}_s^0; \overline{z}_k^2\ {}_t\boldsymbol{\varepsilon}_{*s}^0\right) + \mathbf{Q}_k \frac{\partial}{\partial h}\left(1\,\boldsymbol{\varepsilon}_m^0 + \overline{z}_k\,\boldsymbol{\varepsilon}_b^0 + \overline{z}_k^3\,\boldsymbol{\varepsilon}_{*b}^0 \,\middle|\, 1\,\boldsymbol{\varepsilon}_s^0 + \overline{z}_k^2\,\boldsymbol{\varepsilon}_{*s}^0\right) \tag{48}$$

$$\left(\frac{\partial^{t}\sigma_{I}}{\partial \mathbf{a}}\right)_{k} = \mathbf{Q}_{k}\left(\mathbf{B}_{m} + \bar{z}_{k}\,\mathbf{B}_{b} + \bar{z}_{k}^{3}\,\mathbf{B}_{*b}\middle|\,\mathbf{B}_{s} + \bar{z}_{k}^{2}\,\mathbf{B}_{*s}\right) \tag{49}$$

For FGM structures, the vector distances for each virtual layer k, can be given by the following equations:

$$z_{k+1} = r_{k+1}\frac{h}{2}\ ;\ z_{k} = r_{k}\frac{h}{2} \tag{50}$$

Thus we can write:

$$\frac{z_{k+1}^{n} - z_{k}^{n}}{n} = \left(\frac{r_{k+1}^{n} - r_{k}^{n}}{n}\right)\left(\frac{h}{2}\right)^{n} \tag{51a}$$

where

$$r_{k+1} = \frac{2\,z_{k+1}}{h}\ ;\quad r_{k} = \frac{2\,z_{k}}{h} \tag{51b}$$

The corresponding derivatives are then given by:

$$\frac{\partial z_{k+1} - \partial z_{k}}{\partial h} = \left[r_{k+1} - r_{k}\right]\frac{\partial h}{2\partial h} = \left[r_{k+1} - r_{k}\right]\frac{1}{2}$$

$$\frac{dz_{k+1}^{2} - \partial z_{k}^{2}}{2\,\partial h} = \left[r_{k+1}^{2} - r_{k}^{2}\right]\frac{\partial h^{2}}{8\,\partial h} = \frac{2h}{8}$$

$$\frac{\partial z_{k+1}^{3} - \partial z_{k}^{3}}{3\,\partial h} = \left[r_{k+1}^{3} - r_{k}^{3}\right]\frac{\partial h^{3}}{24\,\partial h} = \left[r_{k+1}^{3} - r_{k}^{3}\right]\frac{3h^{2}}{24}$$

$$\frac{\partial z_{k+1}^{4} - \partial z_{k}^{4}}{4\,\partial h} = \left[r_{k+1}^{4} - r_{k}^{4}\right]\frac{\partial h^{4}}{64\,\partial h} = \left[r_{k+1}^{4} - r_{k}^{4}\right]\frac{4h^{3}}{64}$$

$$\frac{\partial z_{k+1}^{5} - \partial z_{k}^{5}}{5\,\partial h} = \left[r_{k+1}^{5} - r_{k}^{5}\right]\frac{\partial h^{5}}{160\,\partial h} = \left[r_{k+1}^{5} - r_{k}^{5}\right]\frac{5h^{4}}{160}$$

$$\frac{\partial z_{k+1}^{6} - \partial z_{k}^{6}}{6\,\partial h} = \left[r_{k+1}^{6} - r_{k}^{6}\right]\frac{\partial h^{6}}{384\,\partial h} = \left[r_{k+1}^{6} - r_{k}^{6}\right]\frac{6h^{5}}{384}$$

$$\frac{\partial z_{k+1}^{7} - \partial z_{k}^{7}}{7\,\partial h} = \left[r_{k+1}^{7} - r_{k}^{7}\right]\frac{\partial h^{7}}{896\,\partial h} = \left[r_{k+1}^{7} - r_{k}^{7}\right]\frac{7h^{6}}{896} \tag{52}$$

or in a general form:

$$\frac{\partial}{\partial h}\left(\frac{z_{k+1}^{n}-z_{k}^{n}}{n}\right)=\left(r_{k+1}^{n}-r_{k}^{n}\right)\frac{\partial}{\partial h}\left(\frac{h}{2}\right)^{n}=\left(r_{k+1}^{n}-r_{k}^{n}\right)\frac{n h^{n-1}}{n\,2^{n}}\quad . \tag{53}$$

Also, the distance to the mid-plan of the virtual layer k, can be written in the form:

$$\bar{z}_{k}=\frac{z_{k+1}+z_{k}}{2}=\bar{r}_{k}\,\frac{h}{2} \tag{54a}$$

where

$$\bar{r}_{k}=\frac{2\bar{z}_{k}}{h}=\frac{z_{k+1}+z_{k}}{h} \tag{54b}$$

Thus for the derivatives we have:

$$\frac{\partial \bar{z}_{k}}{\partial h}=\frac{\bar{r}_{k}}{2}\;;\;\frac{\partial(\bar{z}_{k})^{2}}{\partial h}=\bar{r}_{k}^{2}\;h\;;\;\frac{\partial(\bar{z}_{k})^{3}}{\partial h}=\frac{3\,\bar{r}_{k}^{3}\,h^{2}}{8}\,. \tag{55}$$